

Energy symmetry and interlayer wave function ratio of tunneling electrons in partially overlapped graphene

Ryo Tamura

Faculty of Engineering, Shizuoka University, 3-5-1 Johoku, Hamamatsu 432-8561, Japan

(Dated: January 23, 2025)

Oscillations of tunneling probability concerning the tunneling barrier thickness have been less studied than the decay length. In this paper, we theoretically study the dependence of the tunneling probability on the electron energy E and barrier thickness, or overlap length, in partially overlapped graphene where a gap is formed only in the central bilayer region due to a perpendicular electric field. We compare an \uparrow junction, where the current path must pass through interlayer states, with a \downarrow junction, where such interlayer transmission is not required. The valley-reversed tunneling probability of the \uparrow junction is symmetric concerning E , whereas other tunneling probabilities are not. Additionally, the valley valve effect spans the entire energy gap in double \uparrow junctions, whereas it occurs only within a much narrower energy range in double \downarrow junctions. Surprisingly, these results suggest that the interlayer wavefunction ratio β has a more significant effect in the \downarrow junction than in the \uparrow junction. This can be understood through the energy symmetry arising from chirality operation, π rotation, and probability conservation. This energy symmetry offers a new perspective for analyzing the effects of β .

I. INTRODUCTION

Tunneling electrons do not possess a real momentum and manifest themselves in nuclear fusion [1], scanning tunneling microscopes [2], tunnel diodes [3], and tunnel magnetic resistance (TMR) [4]. In the barrier region, the component k_x of the wave vector normal to the barrier consists of not only the imaginary part k_x^{im} , which determines the decay length but also the real part k_x^{re} that causes the tunneling probability to oscillate with the barrier thickness. Though the oscillation has been observed in the TMR [5] and theoretically predicted in the side-contacted armchair nanotubes [6, 7], the partially overlapped graphene is more suitable for the systematic survey [8–26]. As Fig. 1 shows, the vertical electric field induces an energy gap in the central overlapping region, but the monolayer regions remain gapless [27–30]. The advanced layer arrangement technique allows us to control the overlap length, i.e., the barrier thickness [31]. Additionally, the dual-gate electrodes allow real-time tuning of the gap width and Fermi level [32–34]. Contrary to the k_x corresponding to the layer-parallel electron motion, it is unclear how the interlayer wave function ratio β influences the tunneling current. The present paper proposes β detection in the energy gap by comparing \downarrow and \uparrow junctions illustrated in Fig. 1. Studies on the tunneling conduction in Refs. [10, 25, 35–37] do not address the β effect. When traveling from the left to the right monolayer region, the electron inevitably passes the interlayer path in the \uparrow junction. Still, it can keep to the lower layer path in the \downarrow junction, leading to the naive expectation that the β effect is weak compared to the \uparrow junction. This paper demonstrates that reality contradicts this expectation, where the symmetry associated with the sign inversion of the electron energy E plays a crucial role.

In the AB sublattice structure, the operation that flips the sign of the wave function on only one of the sublattices

is referred to as a chiral operation, and its generalizations have also been studied [38, 39]. Chiral operations result in the simultaneous reversal of signs for E and the interlayer potential difference ε . As shown in Fig. 1, the sign inversion of ε is equivalent to reversing the z axis normal to the layers. When the z axis inversion follows the chiral operation, k_x remains unchanged, but E and β transform into $-E$ and $-\beta^{-1}$, respectively. With this transformation, this paper reveals the self-cancellation of β in the \uparrow junction.

In the same way as the ballistic electrons, the tunneling electrons can be classified based on whether k_x^{re} is near the K_+ or K_- corner points in the Brillouin zone, namely K_+ or K_- valleys, closely related to valley Hall effect [29, 30, 40–44], valley splitter [34, 45, 46], valley filter (VF), valley reversal, valley bulb (VB), and optical valley selection [47–54]. VF converts a non-valley-polarized current into a current that predominantly contains electrons from one valley [55–63]. VB is a technique that utilizes valley-dependent transmission to suppress current flow. Although alternative methods exist [34, 62], VB can be realized by connecting VF with opposite polarities in series [64, 65]. Valley-reversed transmission refers to the process in which electrons transmit after the valley has been reversed [66–68]. These valley functionalities are interrelated. For instance, valley reversal and VF can sometimes appear simultaneously [7, 37, 56, 62].

Many reports have been on one-dimensional channels localized at the edges [56, 69–72] and at the interfaces. The interfaces are formed by quadrupolar gate electrodes [73–80], stacking difference [81–85], and the alternating sublattice site energy [86, 87]. While the channel-direction components of the wave vector are real in these gapped states, they become complex numbers in the bulk gapped states considered in this paper. The number of edge or interface states contributing to the current corresponds to the Chern number, which originates from the topological properties of the wave function in momentum

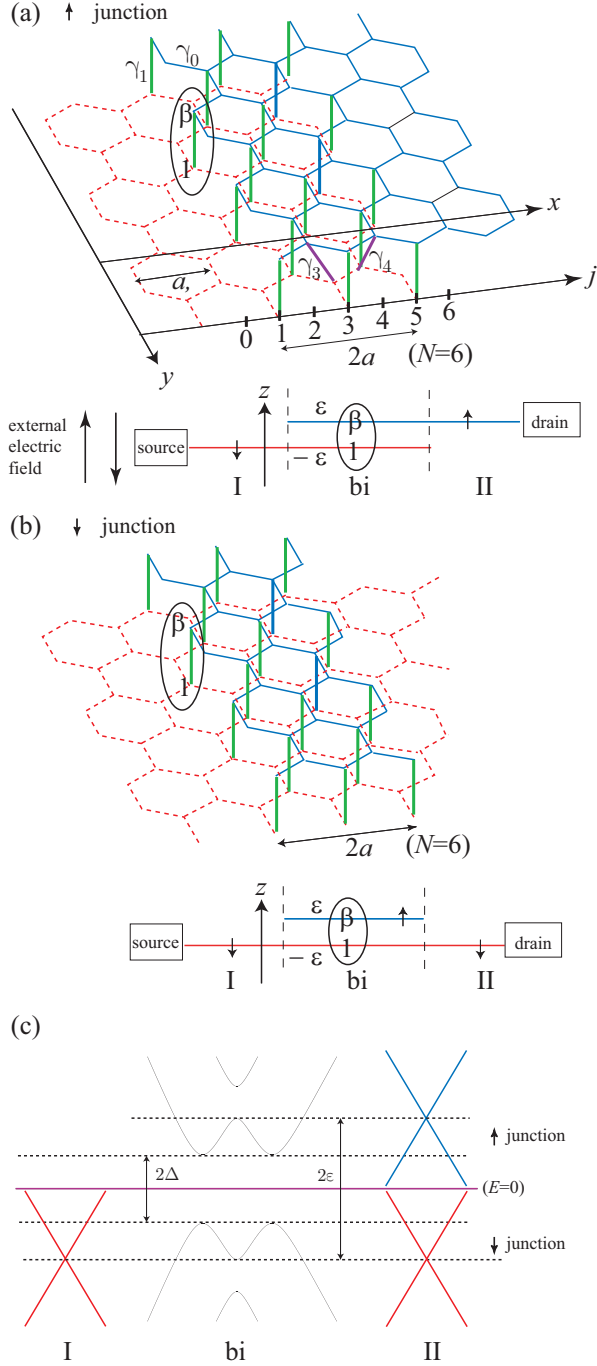


FIG. 1. (a) \uparrow and \downarrow junctions of partially overlapped graphene. Regions I and II represent the left and right monolayer regions, respectively, while bi denotes the central bilayer region. The length of the overlapping region is expressed as $(N-2)\frac{a}{2}$, where N is an integer, and a is the lattice constant. As an example, the case of $N = 6$ is illustrated. A vertical electric field applied via the top and bottom gate electrodes induces an interlayer site energy difference of 2ε . β represents the interlayer ratio of the wave function.

(b) Dispersion curves in regions I, bi, and II at $k_y = 0$. In region bi, an energy gap with a width of 2Δ emerges due to the interlayer site energy difference 2ε , while regions I and II remain gapless. The K -point energy in region II is shifted by 2ε relative to region I in the \uparrow junction, but it remains identical in the \downarrow junction.

space [88–90]. Even in one-dimensional systems where the Chern number is not well-defined, the bulk-edge correspondence can still hold if chiral symmetry is present [91, 92]. When the barrier is thin, and the transmission rate approaches 1, the tunneling current is proportional to the spatial width of the system. In contrast, the edge current is independent of the width. This paper focuses on cases where the system width is large, and the tunneling current dominates, making the bulk-edge correspondence irrelevant. Nevertheless, the chiral symmetry remains crucial due to its role in the β effect.

This paper is organized as follows. Section II presents two types of tight binding models (TB) used in this study: the $\gamma_1\gamma_3\gamma_4$ -model and the γ_1 -model. The simplified γ_1 -model, derived from the $\gamma_1\gamma_3\gamma_4$ -model, allows us to analytically determine the wave functions in Section III and the transmission coefficient in Section IV. In Section V, by considering chiral operation and π rotation in conjunction with the unitarity of the scattering matrix, we prove that the valley-reversed transmission coefficient in the \uparrow junction is an even energy function. Section VI compares the analytical results obtained through this approach with the exact numerical results from the $\gamma_1\gamma_3\gamma_4$ -model, demonstrating their validity. Additionally, we discuss the VB that occurs when the two junctions are connected in series. Section VII provides a summary. Appendix A highlights that the branch cut of the complex square root occurs where the phase is π . Appendix B supplements the calculations presented in Section IV.

II. TIGHT BINDING MODEL

Figure 2 shows how integer labels (j, j_y) and sublattices (A, B) are assigned to the atoms. When $x = j\frac{a}{2}$ is fixed, y_A increases by $\sqrt{3}a$ for every increment of 1 in j_y , and $y_B = y_A - \circ\frac{a}{\sqrt{3}}$, where a denotes the lattice constant, and \circ is a wild card that represents either layer symbols (\downarrow, \uparrow) or integers ($+1, -1$). One mode corresponds to the other mode as

$$\circ = \begin{cases} \downarrow = +1 \\ \uparrow = -1 \end{cases} \quad (1)$$

followed by interpretation $-\downarrow = \uparrow$, $-\uparrow = \downarrow$. With j_y fixed, the y_A is $\frac{\sqrt{3}}{2}a$ smaller for odd j than for even j . These labels allow us to express the wave function as A_{\circ, j, j_y} or B_{\circ, j, j_y} . The TB equation for the bilayer region is represented by

$$E\vec{d}_{\circ, j} = \begin{pmatrix} \gamma_1 & \gamma_4 \\ \gamma_4 & \frac{\gamma_3}{\omega^{2\circ}} \end{pmatrix} \vec{d}_{-\circ, j} + \omega^{-\circ} \begin{pmatrix} 0 & \gamma_4 \\ \gamma_4 & \gamma_3 \end{pmatrix} \vec{d}'_{-\circ, j} - \begin{pmatrix} \circ\varepsilon & 1 \\ 1 & \circ\varepsilon \end{pmatrix} \vec{d}_{\circ, j} - \begin{pmatrix} 0 & \omega^{\circ} \\ \omega^{-\circ} & 0 \end{pmatrix} \vec{d}'_{\circ, j}, \quad (2)$$

where

$$\vec{d}_{\circ, j} = (\sqrt{\omega})^{(-1)^{j+1}} (A_{\circ, j, 0}, B_{\circ, j, 0}),$$

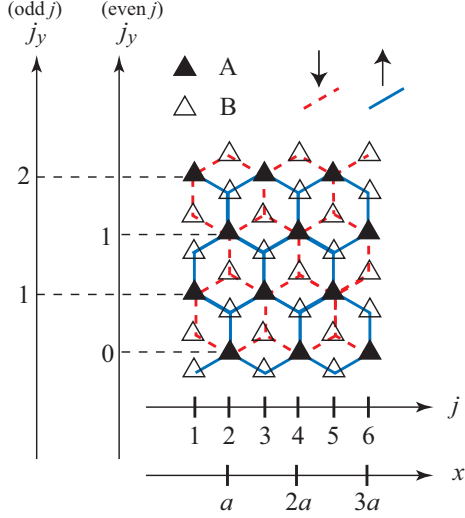


FIG. 2. Integers j and j_y are assigned along the x axis and y axis, respectively, to represent atomic positions. Sublattices are labeled A and B, while the layers are labeled \uparrow and \downarrow . The vertical interlayer transfer integral γ_1 connects the A_{\downarrow} site and the A_{\uparrow} site.

$$\vec{d}'_{\circ,j} = \vec{d}_{\circ,j-1} + \vec{d}_{\circ,j+1}, \quad \omega = e^{i\frac{\sqrt{3}}{2}k_y a},$$

and the intralayer nearest neighbor transfer integral γ_0 is negative as $\gamma_0 = -|\gamma_0| = -1 = -3.12$ eV [93]. The absolute value of γ_0 is the energy unit except when 'eV' appears explicitly. There are two ways to define the sublattices in bilayer graphene. One definition assigns the lattice points such that the vertical interlayer transfer integral γ_1 occurs between A sites, while the other assigns them such that it occurs between AB sites. The chiral operation transforms (A_{\circ}, B_{\circ}) into $(\circ A_{\circ}, -\circ B_{\circ})$ under the former definition, and into $(A_{\circ}, -B_{\circ})$ under the latter. This paper adopts the former definition since it is suitable for treating the \uparrow and \downarrow layers symmetrically.

We obtain the TB equation for the monolayer regions by replacing all the interlayer transfer integrals with zero. We assume that the y component of the wave vector k_y is a good quantum number, and thus $A_{\circ,j,j_y} = \omega^{2j_y} A_{\circ,j,0}$ and $B_{\circ,j,j_y} = \omega^{2j_y} B_{\circ,j,0}$. We use two π orbital TB models. In the $\gamma_1\gamma_3\gamma_4$ -model, $\gamma_1 = 0.377$ eV, $\gamma_3 = 0.29$ eV, and $\gamma_4 = 0.12$ eV [93]. The γ_1 -model is the same as the $\gamma_1\gamma_3\gamma_4$ -model except that $\gamma_3 = \gamma_4 = 0$. The energy E is the Fermi level for the transport. The external vertical electric field induces non-zero ε . They are under the control of dual gate electrodes.

III. WAVE FUNCTION FOR A GENERAL k_y CALCULATED WITH THE γ_1 -MODEL

We designate the right monolayer region with the symbol \bullet , which also follows the rule (1), and refer to the junction between the \bullet and \downarrow layers as the \bullet junction. When

$\gamma_3 = \gamma_4 = 0$, the general solution of the TB equation for the \bullet junction is represented by

$$\vec{d}_{\downarrow,j}^{\text{I}} = \sum_{\nu=\pm} \sum_{\varsigma=\pm} \frac{1}{\sqrt{J_{\nu,\downarrow}}} \xi_{\nu,\text{I}}^{(\varsigma)} \tilde{\lambda}_{\nu,\downarrow}^{\varsigma\nu j} \begin{pmatrix} \tilde{f}_{\nu,\downarrow} \\ 1 \end{pmatrix} \quad (3)$$

in the left monolayer region I ($j \leq 0$),

$$\vec{d}_{\bullet,j}^{\text{II}} = \sum_{\nu'=\pm} \sum_{\varsigma=\pm} \frac{1}{\sqrt{J_{\nu',\bullet}}} \xi_{\nu',\text{II}}^{(\varsigma)} \tilde{\lambda}_{\nu',\bullet}^{\varsigma\nu'(j-N)} \begin{pmatrix} \tilde{f}_{\nu',\bullet} \\ 1 \end{pmatrix} \quad (4)$$

in the right monolayer region II ($j \geq N$), and

$$\begin{pmatrix} \vec{d}_{\downarrow,j}^{\text{bi}} \\ \vec{d}_{\uparrow,j}^{\text{bi}} \end{pmatrix} = \sum_{\tau=\pm} \sum_{l=\pm} \sum_{\varsigma=\pm} \eta_{\tau,l}^{(\varsigma)} \lambda_{\tau,l}^{\varsigma j} \begin{pmatrix} f_{\tau,\downarrow,l} \\ 1 \\ \rho_{\tau,l} \beta_l f_{\tau,\uparrow,l} \\ \rho_{\tau,l} \beta_l \end{pmatrix} \quad (5)$$

in the bilayer region ($1 \leq j \leq N-1$), where the overlap length is $(N-2)\frac{a}{2}$. The sublattice wave function ratio is

$$\tilde{f}_{\nu,\circ} = \frac{\circ(E + \circ\varepsilon)\omega^{\circ}}{\nu \frac{\varepsilon}{|\varepsilon|} \sqrt{(E + \circ\varepsilon)^2 - s^2 - is}} \quad (6)$$

in Eqs. (3) and (4), and

$$f_{\tau,\circ,l} = \frac{\circ(E + \circ\varepsilon)\omega^{\circ}}{\circ\tau \sqrt{p + liq - s^2 - is}} \quad (7)$$

in Eq. (5) with notations

$$p = E^2 + \varepsilon^2, \quad q = \sqrt{(4\varepsilon^2 + \gamma_1^2)(\Delta^2 - E^2)}, \quad (8)$$

and $s = \sin\left(\frac{\sqrt{3}}{2}k_y a\right)$. We consider the gap region $|E| < \Delta$, where $\Delta = \frac{\gamma_1|\varepsilon|}{\sqrt{4\varepsilon^2 + \gamma_1^2}}$ stands for the half energy gap width [27, 28, 93, 94]. ξ (η) denotes the mode amplitudes of the monolayer (bilayer) regions. The interlayer wavefunction ratio is expressed as the product of

$$\rho_{\tau,l} = \omega^2 \frac{\tau \sqrt{p - s^2 + ilq + is}}{\tau \sqrt{p - s^2 + liq - is}} \quad (9)$$

and

$$\beta_l = \frac{2\varepsilon E - ilq}{\gamma_1(E - \varepsilon)}. \quad (10)$$

The condition that Eqs. (3) and (4) must be in an extended state determines s_{max} , the maximum allowable s as

$$s_{\text{max}} = \begin{cases} |E + \varepsilon| & \cdots \downarrow \text{ junction} \\ ||E| - |\varepsilon|| & \cdots \uparrow \text{ junction} \end{cases} \quad (11)$$

Equation (7) determines the Bloch phase factor factors $\lambda_{\tau,l}$ in Eq. (5) as

$$\lambda_{\tau,l} = \mu + \sqrt{\mu^2 - 1}, \quad (12)$$

where

$$\mu = -\frac{\omega^\circ}{2} \left(1 + \frac{E + \circ\varepsilon}{f_{\tau,\circ,l}} \right). \quad (13)$$

Although $f_{\tau,\circ,l}$ depends on the layer index \circ , $\lambda_{\tau,l}$ does not depend on \circ . Replacing f with \tilde{f} in Eq.(13), we obtain the Bloch phase factor $\tilde{\lambda}$ in Eqs. (3) and (4). $J_{\pm,\circ}$ denotes $\text{Re}(\omega^{-\circ} \tilde{f}_{\pm,\circ}) \text{Im}(\tilde{\lambda}_{\pm,\circ})$, and the probability flow equals $\sum_\nu |\xi_\nu^{(+)}|^2 - |\xi_\nu^{(-)}|^2$. $|\tilde{\lambda}| = 1$ for the monolayer region, while $|\lambda| < 1$ for the bilayer region. The superscript ς of ξ (η) represents the propagation (decay) direction.

By relating the TB equation to the Dirac equation under the effective mass approximation, f and \tilde{f} represent the orientations of a pseudospin [95–97]. At the interfaces I-bi and bi-II, less variation in pseudospin leads to higher transmission rates. Therefore Eqs. (6) and (7) indicate that the bilayer mode τ is dominant in the transmission under conditions

$$\tau = \frac{\varepsilon}{|\varepsilon|} \nu = \bullet \frac{\varepsilon}{|\varepsilon|} \nu', \quad (14)$$

and $(E \pm \varepsilon)^2 \simeq p + liq$. The following identity demonstrates that the latter condition is satisfied when $|\varepsilon| \gg \gamma_1$.

$$\left| \frac{(E \pm \varepsilon)^2}{p \pm iq} - 1 \right|^2 = \frac{\gamma_1^2}{\varepsilon^2 + \gamma_1^2 - E^2} \quad (15)$$

Reflecting Eq.(14), $T_{\bullet,\nu,\nu} \gg T_{\bullet,\nu,-\nu}$. The mode that satisfies $\tilde{d}_{j+1} \simeq e^{\pm i\frac{2}{3}\pi} \tilde{d}_j$ is designated as the K_\pm valley mode. This valley classification correlates with the x axis orientation choice. Since $\tilde{\lambda} \simeq e^{i\frac{2}{3}\pi}$, the $\xi_{\nu,\circ}^{(\varsigma)}$ mode corresponds to the $K_{\varsigma\nu}$ -valley mode, and ν serves as a valley index. We introduce notation $\lambda_\tau \equiv \lambda_{\tau,+}$ and

$$\lambda_\tau = |\lambda_\tau| e^{i(\phi_\tau + \tau\frac{2}{3}\pi)} \quad (16)$$

where ϕ_τ signifies the relative phase shift of λ_τ with respect to $\tau\frac{2}{3}\pi$. Note that $\lambda_{\tau,-} = \lambda_\tau^*$. We prove that $|\lambda_\tau| < 1$ and $|\phi_\tau| \ll 1$ in Appendix A. Equation (16) illustrates that the valley of mode $\eta_{\tau,l}^{(\varsigma)}$ becomes $K_{\varsigma\tau l}$. The degree of freedom l corresponds to complex conjugation and is independent of ς . Complex conjugation correlates with reversing the propagation direction in a propagating wave, but it becomes independent of the decay direction in a decaying wave.

The valley conservation ($\nu = \nu'$) and valley reversal ($\nu = -\nu'$) manifest themselves in the \downarrow and \uparrow junctions, respectively, in Eq. (14). With abbreviation $\eta_1 = \eta_{\tau,+}^{(+)}$, $\eta_2 = \eta_{\tau,+}^{(-)}$, $\eta_3 = \eta_{\tau,-}^{(+)}$, $\eta_4 = \eta_{\tau,-}^{(-)}$, $\lambda = \lambda_{\tau,+}$ and $\beta = \beta_+$, we approximate Eq. (5) as

$$\begin{pmatrix} \tilde{d}_{\downarrow,j}^{\text{bi}} \\ \tilde{d}_{\uparrow,j}^{\text{bi}} \end{pmatrix} \simeq \sum_{\nu=\pm} \begin{pmatrix} g_\downarrow(j) \begin{bmatrix} \tilde{f}_{\nu,\downarrow} \\ 1 \end{bmatrix} \\ \omega^2 g_\uparrow(j) \begin{bmatrix} \tilde{f}_{-\nu,\uparrow} \\ 1 \end{bmatrix} \end{pmatrix} \Bigg|_{\tau=\frac{\varepsilon}{|\varepsilon|}\nu} \quad (17)$$

$$g_\downarrow(j) = \eta_1 \lambda^j + \eta_2 \lambda^{-j} + \eta_3 (\lambda^*)^j + \eta_4 (\lambda^*)^{-j} \quad (18)$$

$$g_\uparrow(j) = \beta(\eta_1 \lambda^j + \eta_2 \lambda^{-j}) + \beta^*(\eta_3 (\lambda^*)^j + \eta_4 (\lambda^*)^{-j}) \quad (19)$$

under the conditions $|\varepsilon| \gg \gamma_1$ and $|s| \ll |\sqrt{p - s^2 + iq}|$. Limiting τ to Eq. (14), we suppress τ except when we had better show τ explicitly.

Suppose $N \gg 1$ and the K_ν electron is incident from region I. The wave function (17) decays with j except when j is very close to N . It is equivalent to condition $|\eta_2|, |\eta_4| \ll |\eta_1|, |\eta_3|$. Applying this condition to the boundary condition $g_\uparrow(0) = 0$, we derive

$$\frac{\eta_3}{\eta_1} = -\frac{\beta}{\beta^*}. \quad (20)$$

Using Eqs. (20), $g_{-\bullet}(N) = 0$, and

$$g_{\bullet}(N) = e^{\nu' i\frac{2}{3}\pi} g_{\bullet}(N-1), \quad (21)$$

we obtain

$$\frac{\eta_2}{\eta_1} = \frac{\beta}{\beta^*} |\lambda|^{2N} + \delta_{\uparrow,\bullet} \left(\frac{\beta}{\beta^*} - 1 \right) \lambda^{2N} \quad (22)$$

and

$$\frac{\eta_4}{\eta_1} = -\frac{\beta}{\beta^*} \left[|\lambda|^{2N} + \delta_{\downarrow,\bullet} \left(\frac{\beta}{\beta^*} - 1 \right) (\lambda^*)^{2N} \right]. \quad (23)$$

In the derivation of Eqs. (22) and (23), we use approximation $\lambda_\tau \simeq e^{i\tau\frac{2}{3}\pi}$ and $\tilde{\lambda} \simeq e^{i\frac{2}{3}\pi}$. However we cannot replace λ_τ^N with $e^{i\tau\frac{2}{3}\pi N}$, because $N \gg 1$. When j is not close to N ,

$$(|g_\downarrow(j)|, |g_\uparrow(j)|) \simeq 2|\beta\eta_1| (|\text{Im}(\beta^{-1}\lambda^j)|, |\text{Im}(\lambda^j)|) \quad (24)$$

holds. At the output interface $j = N$,

$$(|g_\downarrow(N)|, |g_\uparrow(N)|) = 4|\text{Im}(\beta)\eta_1| (|\text{Re}(\beta^{-1}\lambda^N)|, 0) \quad (25)$$

for the \downarrow junction, and

$$(|g_\downarrow(N)|, |g_\uparrow(N)|) = 4|\text{Im}(\beta)\eta_1| (0, |\text{Re}(\lambda^N)|) \quad (26)$$

for the \uparrow junction. When Eqs. (24), (25), and (26) are compared, it is apparent that the wave function exhibits a phase shift of $\frac{\pi}{2}$ between the entrance and the exit.

IV. TRANSMISSION RATE FOR ZERO- k_y CALCULATED WITH THE γ_1 -MODEL

We discuss the transmission rate $T_{\nu',\nu}$ from the K_ν to the $K_{\nu'}$. Using the γ_1 -model at $k_y = 0$ to derive the analytical expression, Ref. [68] obtained it in the band

region $\Delta < |E| < |\varepsilon|$, and Ref. [37] derived it in the gap region $|E| < \Delta$ as

$$T_{\nu',\nu} = \left| \left(\tilde{t} \cdot \Lambda^N \sum_{n=0}^{\infty} (r_{\downarrow} \Lambda^N r_{\bullet} \Lambda^N)^n t_{\downarrow} \right)_{\nu',\nu} \right|^2, \quad (27)$$

where n signifies the number of times the wave travels back and forth across the bilayer region, and $\Lambda = \text{diag}(\lambda_{+,+}, \lambda_{-,+}, \lambda_{-,-}, \lambda_{+,-})$. We obtain λ for the band region by replacing iq by $|q|$ in Eq. (7). t (\tilde{t}) denotes the transmission matrix at the entrance (exit) interface. Matrixes r represent the reflection. Subscript \downarrow (\bullet) corresponds to the entrance (exit). In the band region, $|\lambda| = 1$, and thus, we cannot neglect multiple reflection terms with $n \geq 1$ in Eq. (27). In the gap region, however, $|\lambda| < 1$, and Eq. (27) is approximated by

$$T_{\nu',\nu} = \left| (\tilde{t} \cdot \Lambda^N t_{\downarrow})_{\nu',\nu} \right|^2, \quad (28)$$

when $N \gg 1$. Equation (28) can be approximated for the dominant path (14) as follows.

$$T_{\bullet\nu,\nu} = \frac{\gamma_1^6}{q^6} (\varepsilon^2 - E^2)^2 \frac{Z_{\bullet\nu,\nu}^2}{|\zeta_{\bullet,+} \zeta_{\bullet,-} \zeta_{\downarrow,+} \zeta_{\downarrow,-}|^2} \quad (29)$$

where

$$Z_{\nu,\nu} = \frac{1}{\sqrt{p}} (|E + \varepsilon| + \sqrt{p})^2 \text{Re}(\beta^{-1} \lambda_{\tau}^N) \Big|_{\tau = \frac{\varepsilon}{|\varepsilon|} \nu} \quad (30)$$

for the $\bullet = \downarrow$ junction,

$$Z_{-\nu,\nu} = 2\varepsilon \left(1 + \frac{|\varepsilon|}{\sqrt{p}} \right) \text{Re}(\lambda_{\tau}^N) \Big|_{\tau = \frac{\varepsilon}{|\varepsilon|} \nu} \quad (31)$$

for the $\bullet = \uparrow$ junction, and

$$\zeta_{\circ,\pm} = 1 + \frac{(E + \circ\varepsilon)^{\pm 1}}{iq} \text{Re} \left(\frac{\circ 2\varepsilon E + iq}{(\sqrt{p} + iq)^{\pm 1}} \right). \quad (32)$$

Appendix B shows the derivation of (29). The Re factors in Eqs. (30) and (31) are represented by

$$\text{Re} \left(\frac{\lambda_{\frac{\varepsilon}{|\varepsilon|} \nu}^N}{\beta^{\delta_{\bullet,\downarrow}}} \right) = \frac{|\lambda_{\tau}|^N}{|\beta^{\delta_{\bullet,\downarrow}}|} \cos \left(\tau \frac{2}{3} \pi N + \phi_{\tau} N - \varphi \delta_{\bullet,\downarrow} \right) \Big|_{\tau = \frac{\varepsilon}{|\varepsilon|} \nu} \quad (33)$$

where φ denotes the phase of β .

V. ENERGY SYMMETRY FOR THE \uparrow JUNCTION

This section proves the energy symmetry of the inter-valley transmission rates for the \uparrow junction. This symmetry exactly holds in the γ_1 -model, and Eqs. (3) and (4)

can be employed for this proof. In this section, however, Eqs. (3) and (4) are approximated as

$$\vec{d}_{\circ,j}^{\text{I}} = \sum_{\nu=\pm} \left(\xi_{\nu,\text{I}}^{(+)} \Omega^{\nu j} + \xi_{\nu,\text{I}}^{(-)} \Omega^{-\nu j} \right) \begin{pmatrix} \nu \\ \iota_2 \end{pmatrix} \quad (34)$$

$$\vec{d}_{\circ,j}^{\text{II}} = \sum_{\nu=\pm} \left(\xi_{\nu,\text{II}}^{(+)} \Omega^{\nu(j-N)} + \xi_{\nu,\text{II}}^{(-)} \Omega^{-\nu(N-j)} \right) \begin{pmatrix} \nu \iota_2 \\ 1 \end{pmatrix} \quad (35)$$

for perspicuity, where $\Omega = e^{i\frac{2}{3}\pi}$. We omit $1/\sqrt{J}$ and replace $\tilde{\lambda}_{\nu,\circ}$ and $\tilde{f}_{\nu,\circ}$ with Ω and ν , respectively. In Fig. 3, $(\iota_1, \iota_2)_{\circ}$ denotes the system defined by Eqs. (34) and (35) with the layer index \circ of region I and a pair of signs (ι_1, ι_2) , where $(+, +)_{\downarrow}$ is the original \uparrow junction. The x axis inversion transforms $(+, +)_{\downarrow}$ into $(-, +)_{\uparrow}$, replacing j with $N - j$ in Eqs. (34) and (35). Here, we fix labels I and II but change (\downarrow, \uparrow) allocation such that the direction from \downarrow to \uparrow aligns with the positive direction of the x axis. If the z axis is taken to point from the lower layer to the upper layer, this operation is equivalent to a π rotation about the y axis. Comparing $(+, +)_{\downarrow}$ and $(-, +)_{\uparrow}$, E is common, but ε has opposite signs, where ε denotes the site energy of the \uparrow side. Under the chiral operation $(A_{\circ}, B_{\circ}) \rightarrow (-\circ A_{\circ}, \circ B_{\circ})$, $(-, +)_{\uparrow}$ changes into $(-, -)_{\uparrow}$, with the reversal of E and ε signs. $(-, -)_{\uparrow}$ has the same ε sign as the original system $(+, +)_{\downarrow}$ because the sign changes two times. The transmission and reflection in $(+, +)_{\downarrow}$ is represented by

$$\begin{pmatrix} \vec{\xi}_{\text{I}}^{(-)} \\ \vec{\xi}_{\text{I}}^{(+)} \end{pmatrix} = S(E, \varepsilon) \begin{pmatrix} \vec{\xi}_{\text{I}}^{(+)} \\ \vec{\xi}_{\text{I}}^{(-)} \end{pmatrix}, \quad (36)$$

where $t_{\text{I}}^{\vec{\xi}(\pm)} = (\xi_{\pm,\text{I}}^{(\pm)}, \xi_{\mp,\text{I}}^{(\pm)})$, and $t_{\text{II}}^{\vec{\xi}(\pm)} = (\xi_{\pm,\text{II}}^{(\pm)}, \xi_{\mp,\text{II}}^{(\pm)})$. We define the rows and columns of the S matrix as

$$S = \begin{pmatrix} S_{-\downarrow,+\downarrow} & S_{-\downarrow,-\downarrow} & S_{-\downarrow,-\uparrow} & S_{-\downarrow,+\uparrow} \\ S_{+\downarrow,+\downarrow} & S_{+\downarrow,-\downarrow} & S_{+\downarrow,-\uparrow} & S_{+\downarrow,+\uparrow} \\ S_{+\uparrow,+\downarrow} & S_{+\uparrow,-\downarrow} & S_{+\uparrow,-\uparrow} & S_{+\uparrow,+\uparrow} \\ S_{-\uparrow,+\downarrow} & S_{-\uparrow,-\downarrow} & S_{-\uparrow,-\uparrow} & S_{-\uparrow,+\uparrow} \end{pmatrix}, \quad (37)$$

where indexes $\pm\circ$ signifies the valley K_{\pm} of the layer \circ . When $\bullet = \uparrow$, Eq. (27) corresponds to the $\uparrow\downarrow$ block of Eq. (37). Irrespective of labels I and II, amplitude $\xi_{\nu}^{(+)}$ ($\xi_{\nu}^{(-)}$) corresponds to the $K_{\nu\iota_1}$ ($K_{-\nu\iota_1}$) valley of which the sign of the probability flow is $\nu\iota_1\iota_2$ ($-\nu\iota_1\iota_2$). The arrows of wavy lines in Fig. 3 indicate the direction of the probability flow. Accordingly, we obtain

$$\begin{pmatrix} \vec{\xi}_{\text{II}}^{(+)} \\ \vec{\xi}_{\text{I}}^{(-)} \end{pmatrix} = S(E, -\varepsilon) \begin{pmatrix} \vec{\xi}_{\text{II}}^{(-)} \\ \vec{\xi}_{\text{I}}^{(+)} \end{pmatrix} \quad (38)$$

for $(-, +)_{\uparrow}$, and

$$\begin{pmatrix} \sigma_x \vec{\xi}_{\text{II}}^{(-)} \\ \sigma_x \vec{\xi}_{\text{I}}^{(+)} \end{pmatrix} = S(-E, \varepsilon) \begin{pmatrix} \sigma_x \vec{\xi}_{\text{II}}^{(+)} \\ \sigma_x \vec{\xi}_{\text{I}}^{(-)} \end{pmatrix} \quad (39)$$

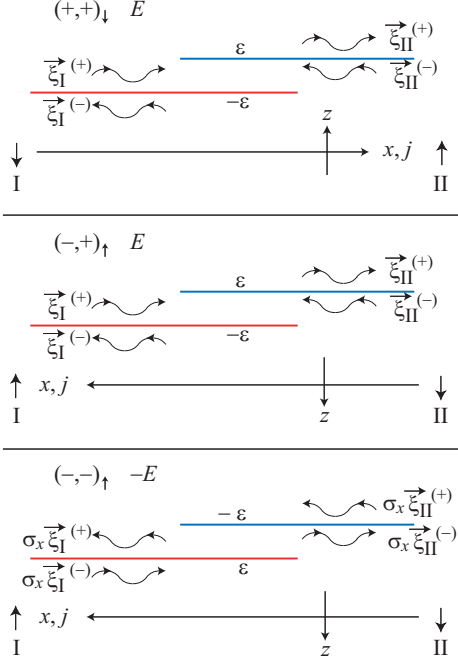


FIG. 3. Operations representing symmetry. The meanings of the symbols $(+,+)\downarrow$, $(-,+)\uparrow$, and $(-,-)\uparrow$ are explained in the main text. The original \uparrow junction $(+,+)\downarrow$ is transformed into $(-,+)\uparrow$ by a π rotation about the y axis. The direction from \downarrow to \uparrow aligns with the positive direction of the x axis. Under the chiral operation, accompanied by the inversion of the signs of E and ε , $(-,+)\uparrow$ changes into $(-,-)\uparrow$. The arrows of wavy lines indicate the direction of the probability flow.

for $(-,-)\uparrow$, where σ_x stands for the Pauli matrix. Since S is unitary, Eqs. (36) and (39) indicate

$$S(-E, \varepsilon) = \begin{pmatrix} 0 & \sigma_x \\ \sigma_x & 0 \end{pmatrix} t S^*(E, \varepsilon) \begin{pmatrix} 0 & \sigma_x \\ \sigma_x & 0 \end{pmatrix} \quad (40)$$

leading to

$$T_{\mp, \pm}(-E, \varepsilon) = T_{\mp, \pm}(E, \varepsilon) \quad (41)$$

for the \uparrow junction. Equation (32) possesses the energy symmetry

$$\zeta_{\downarrow, \pm}(-E, \varepsilon) = \zeta_{\uparrow, \pm}(E, \varepsilon)^*, \quad (42)$$

λ is an even function of E , and thus Eq. (29) for the \uparrow junction satisfies Eq. (41).

VI. RESULTS AND DISCUSSION

The analytical expression becomes less accurate as $|\varepsilon|$ decreases, which is due to the condition $|\varepsilon| \gg \gamma_1$ under which it was obtained. However, when ε changes continuously, the transmission rate does not undergo discontinuous changes. Numerical calculations are necessary

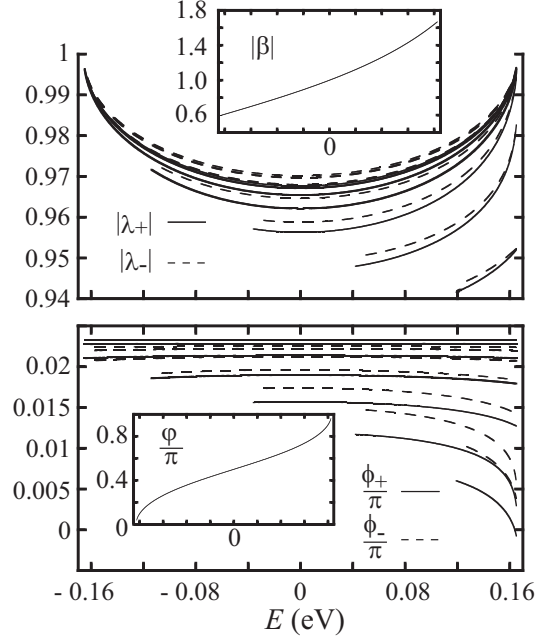


FIG. 4. $|\lambda_{\pm}|$ (upper panel) and ϕ_{\pm}/π (lower panel) for $\varepsilon = 0.35$ eV and $\sqrt{3}k_y a = 0.016m\pi$, where $m = 0, 1, \dots, 6$. The data are plotted for the range $s < |E + \varepsilon|$, where Eq. (3) represents a propagating wave. Both ϕ_{\pm} and $|\lambda_{\pm}|$ decrease with k_y . The solid (dashed) line corresponds to λ_+ (λ_-). For the upper panel, lines $m = 0$ and $m = 1$ are nearly identical. Inset: $|\beta|$ (upper inset) and φ/π (lower inset). The horizontal axis range is identical in all panels and insets.

to verify how large $|\varepsilon|$ must be. Below, we present the results for $\varepsilon = 0.35$ eV, slightly smaller than γ_1 . The corresponding gap width 2Δ is about 0.33 eV. The energy gaps reported in experiments are 0.14 eV [32, 33], 0.16 eV [98], and 0.25 eV [99]. In density functional theory (DFT) calculations that include structural relaxation, the energy gap increases with an electric field but saturates at 0.326 eV [100]. Since DFT calculations tend to underestimate energy gaps, an energy gap of 0.33 eV is feasible. The electric double-layer transistors technology may apply for applying a strong vertical electric field [101]. We employed the method in Ref. [102] for the exact numerical calculations. If the analyzed quantity is an even function of k_y , we implicitly restrict k_y to non-negative values.

Figure 4 shows $|\lambda_{\pm}|$ and the phase shift ϕ_{\pm} defined in Eq. (16), indicating that $\phi_+ \simeq \phi_- \simeq 0$ and $\lambda_+ \simeq e^{i\tau \frac{2}{3}\pi}$. Although $|\lambda_+|$ is very close to $|\lambda_-|$, they differ slightly. Both ϕ_{\pm} and $|\lambda_{\pm}|$ decrease with k_y . In the barrier region, the wave function decays very slowly ($|\lambda| \simeq 1$), and its phase closely corresponds to that of the valley states. The factor $1 + \lambda + \lambda^{-1}$ of mode η is small and, by weakening the effects of γ_3 and γ_4 in Eq. (2), allows the analytical expressions to remain valid within the $\gamma_1\gamma_3\gamma_4$ -model. References [36, 37, 68] have also confirmed the effectiveness of the γ_1 -model.

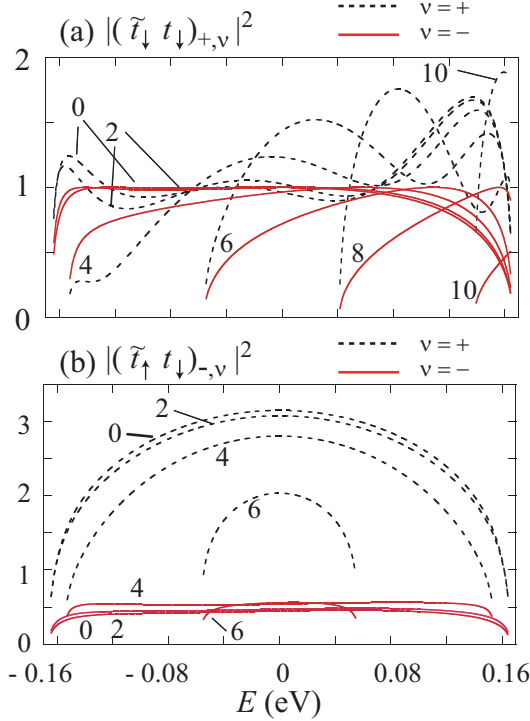


FIG. 5. (a) $C_{\nu',\nu}^{(\downarrow)} \equiv |(\tilde{t}_\downarrow t_\downarrow)_{\nu',\nu}|^2$ and (b) $C_{\nu',\nu}^{(\uparrow)} \equiv |(\tilde{t}_\uparrow t_\uparrow)_{\nu',\nu}|^2$ are shown for $\varepsilon = 0.35$ eV and $\sqrt{3}k_y a = 0.02m\pi$ ($m = 0, 1, 2, \dots$) in the range where s is less than Eq. (11). The attached numbers represent $2m$. The γ_1 -model is used. Since $C_{-,+}^{(\downarrow)} = C_{+,-}^{(\downarrow)}$, $C_{-,-}^{(\downarrow)} \simeq C_{+,+}^{(\downarrow)}$ and $C_{+,\pm}^{(\uparrow)} \simeq C_{-,\mp}^{(\uparrow)}$, we omit $C_{-, \nu}^{(\downarrow)}$ and $C_{+, \nu}^{(\uparrow)}$.

The factor $\text{Re}(\lambda^N \beta^{-\delta_{\bullet,\downarrow}})$ appears both when k_y is finite (Sec. III) and when k_y is zero (Sec. IV). This is reminiscent of the approximation using Eq. (12) in Eqs. (30) and (31) for finite k_y . To confirm the validity of this approximation, Fig. 5 shows the k_y - and E -dependence of $C_{\nu',\nu}^{(\bullet)} \equiv |(\tilde{t}_\bullet t_\bullet)_{\nu',\nu}|^2$ using the γ_1 -model. This factor is extracted from Eq. (28) as the part independent of N . When $k_y = 0$, we can use the analytical expressions demonstrated in Appendix B. For non-zero k_y , however, we have to perform numerical calculations. It remains challenging to derive a clear analytical expression for t_\downarrow and \tilde{t}_\bullet at finite k_y . When k_y is close to zero, the k_y -dependence of the $C^{(\bullet)}$ is small. As s deviates from zero, Eq. (28) diminishes due to the $|\lambda|$ decrease. Since the large T governs the transport, Fig. 5 justifies the approximation of representing the effects of k_y solely through λ by using Eqs. (30) and (31).

Figure 6 shows the dependence of the $T_{\bullet,\nu}$ on E and k_y for the dominant path (14). The dashed line depicts Eq. (29), obtained by applying Eq. (12) to λ , and reproduces the exact result of the $\gamma_1\gamma_3\gamma_4$ -model depicted with the solid line. The length N of the bilayer region is 56, sufficiently long for Eq. (28) to be valid. The most

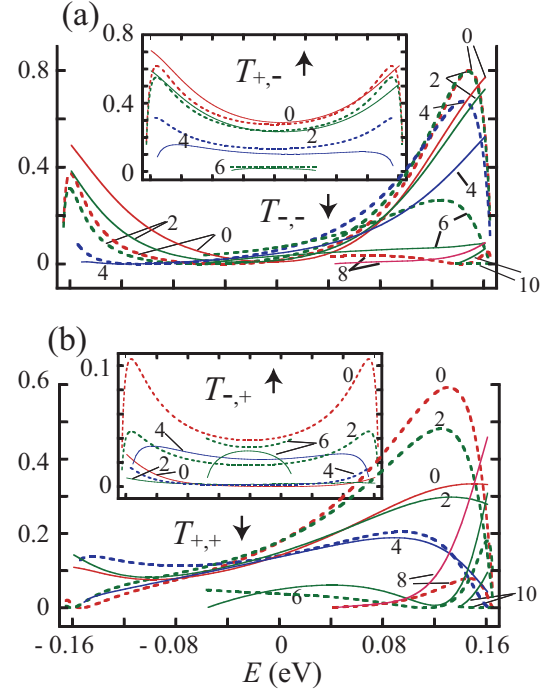


FIG. 6. For the \downarrow junction, (a) $T_{-,-}$, and (b) $T_{+,+}$. Inset: For the \uparrow junction, (a) $T_{+,-}$, and (b) $T_{-,+}$. The attached numbers have the same meaning as in Fig. 5. The bilayer length N is set to 56. The solid lines represent the exact results obtained using the $\gamma_1\gamma_3\gamma_4$ -model, and the dashed lines represent the analytical expressions. The horizontal axis range is identical in all panels and insets.

notable difference between the two types of junctions is that energy symmetry is present in the \uparrow junction but absent in the \downarrow junction. This is attributable to λ^N appearing alone in Eq. (31), whereas in Eq. (30), it appears alongside β^{-1} . As shown in Fig. 4, λ is an even function of E , whereas β is not. The agreement between the solid and dashed lines in the inset of Fig. 6 (b) appears to be worse compared to the inset of Fig. 6 (a). However, the critical point is that the $T_{-,+}$ remains below 0.1 across the entire gap. This is closely related to the energy range where a VB occurs.

The transmission rate T tends to decrease as k_y increases. This reduction is due to the decrease in $|\lambda|$ with increasing k_y , as shown in Fig. 4. Below, we fix k_y at a value smaller than 0.04π and consider cases where changes in $N\phi_\pm$ due to E are negligible. Figure 4 demonstrates that under the former condition, the latter condition is satisfied when $N < 100$. In this scenario, the variation of the cosine function concerning E in Eq. (33) does not occur in the \uparrow junction, whereas in the \downarrow junction, it occurs due to the phase φ . As E increases from $-\Delta$ to Δ , the phase φ increases by π , resulting in zeros of the cosine function for E within the energy gap. These zeros suppress the $T_{\pm,\pm}$ near the edges of the gap in Fig. 6 (b) and around $E = -0.05$ eV in Fig. 6 (a). Due to

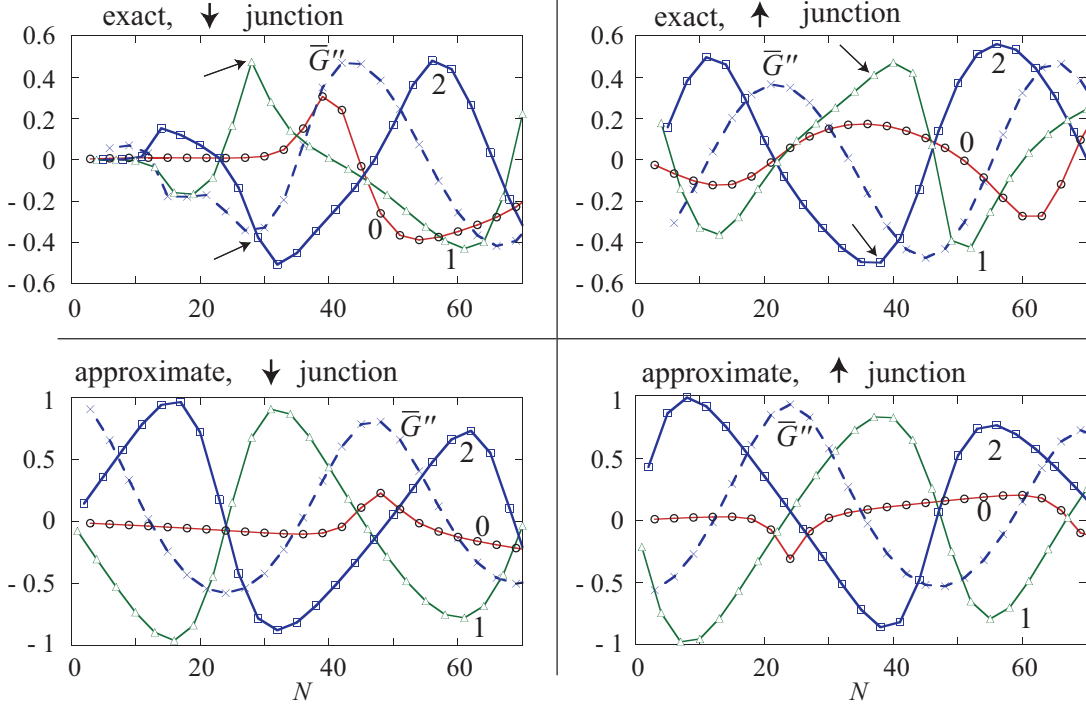


FIG. 7. For zero energy, the solid lines represent the normalized valley conductance \overline{G}_v , and the dashed lines represent the normalized curvature \overline{G}'' of the N - G curve. The definitions of \overline{G}_v and \overline{G}'' are provided in the main text. Circles, triangles, and squares represent \overline{G}_v for cases where $\text{mod}(N) = 0$, $\text{mod}(N) = 1$, and $\text{mod}(N) = 2$, respectively. The system width was set to $N_y = 1000$. The left and right panels correspond to the \downarrow and \uparrow junctions, respectively. The upper and lower panels represent the exact numerical results from the $\gamma_1\gamma_3\gamma_4$ -model, and the results from analytical expressions, respectively.

the significant change in φ within the gap, the suppression of the T across the entire gap does not occur in the \downarrow junction. In contrast, when $N(\phi_\tau + \tau\frac{2}{3}\pi)$ close to an odd multiple of $\frac{\pi}{2}$, $T_{-\nu,\nu}$ becomes nearly zero across the entire gap for the \uparrow junction, where $\nu = \tau\frac{\varepsilon}{|\varepsilon|}$. The $T_{-,+}$ in Fig. 6 (b) shows an example of such $T_{-\nu,\nu}$. For the \uparrow junction, Eq. (33) is independent of φ , and φ does not shield the energy dependence of $|\lambda|$. Both $T_{+,-}$ in Fig. 6 (a) and $|\lambda_-|$ in Fig. 4 decrease as E approaches zero.

The valley-resolved conductance $G_{\nu',\nu}$ is a critical parameter for understanding electronic transport properties. Using Landauer's formula [103], it is calculated by summing the transmission rates over k_y : $G_{\nu',\nu} = \frac{2e^2}{h} \sum_{m=-M}^M T_{\nu',\nu}(m\Delta k_y)$. The periodic boundary condition in the y -direction leads to the discretization of $\Delta k_y = \frac{2\pi}{\sqrt{3}aN_y}$ with the system width $\sqrt{3}aN_y$. In our computations, N_y is taken as 1000. Equation (11) determines M , the maximum allowable integer m , as $s_{\max} = \sin(M\Delta k_y)$. The channel number per valley is then $2M + 1$. Figure 7 shows the normalized valley conductance $\overline{G}_v = \frac{G_v}{G}$ at the gap center $E = 0$, where $G = \sum_{\nu',\nu} G_{\nu',\nu}$ and $G_v = \sum_{\nu} (G_{+, \nu} - G_{-, \nu})$ represent the total conductance and valley conductance, respectively. The phase of the decay factor λ_{\pm} is close to $\pm\frac{2}{3}\pi$ and shows oscillations with a period of 3 in N . Therefore, we plot \overline{G}_v in Fig. 7 with points connected by

lines for each $\text{mod}(N)$ representing the remainder of N divided by three. The left and right panels correspond to the \downarrow and \uparrow junctions, respectively. The lower (upper) panels present the analytic expressions (the exact numerical results from the $\gamma_1\gamma_3\gamma_4$ -model). The minor transmission channels $-T_{\mp\bullet,\pm}$ in the \bullet junction – are neglected in the lower panel. However, they are included in the upper panel, leading to a reduction in the amplitude. Additionally, for small N , terms with $n \geq 1$ in Eq. (27) become significant and cannot be ignored. This is why the upper and lower panels discrepancy is particularly pronounced for $N < 20$ in the \downarrow junction. Except for this point, the analytical expressions closely replicate the oscillation period and the positions of the maxima and minima in the exact results when $\text{mod}(N) \neq 0$. The argument θ of the cosine function in Eq. (33) changes by $\Delta\theta = \left(\frac{4}{3}\frac{\varepsilon}{|\varepsilon|}\pi + \phi_{\frac{\varepsilon}{|\varepsilon|}} - \phi_{-\frac{\varepsilon}{|\varepsilon|}}\right)N$ when the incident valley changes from K_- to K_+ . This $\Delta\theta$ introduces a significant difference between $T_{\bullet,+}$ and $T_{-\bullet,-}$ in the \bullet junction, except when $\Delta\theta$ is close to an integer multiple of π . This explains the differences between $T_{-,-}$ and $T_{+,+}$ and why $T_{+,-}$ is much larger than $T_{-,+}$ in Fig. 6. Reversing the sign of ε changes G_v through $\Delta\theta$. The VF in zigzag graphene ribbons also reverses its polarity depending on the sign of the site energy [55, 62]. When $|\phi_+ - \phi_-|N$ is small, $|\Delta\theta|$ can be approximated as $\frac{4}{3}\pi N$. This accounts

for the smaller amplitude of the solid line for $\text{mod}(N) = 0$ compared to $\text{mod}(N) \neq 0$ in Fig. 7.

Intriguingly, both the junctions exhibit G_v with the same sign in Fig. 7, despite the valley reversal occurring only in the \uparrow junction. At zero energy, β equals i , causing a phase shift of $\varphi = \frac{\pi}{2}$ in Eq. (30) relative to Eq. (31). Since the transmission rate is proportional to the square of Eqs. (30) and (31), the sign reversal occurs, canceling out the effect of the valley reversal. However, as E moves away from zero, β deviates from i , causing this cancellation to become imperfect. At zero energy, differences due to the type of junction do not manifest in valley selectivity in this way, but they do appear in the curvature of the N - G curve, $G''(N) = G(N+1) + G(N-1) - 2G(N)$. The dashed line in Fig. 7 represents the normalized curvature $\overline{G}''(N) = G''(N)/[G(N+1) + G(N-1) + 2G(N)]$ for the case where $\text{mod}(N) = 0$. By applying $\varphi = \frac{\pi}{2}$ and $\phi_+ \simeq \phi_-$ to Eq. (33), the resulting $\overline{G}'' = \bullet 3 \cos(2N\phi)/(4 - \bullet \cos(2N\phi))$ acquires opposite signs in the \downarrow and \uparrow junctions, as Fig. 7 depicts. Interestingly, the phase of the N - \overline{G}_v curve is shifted by $\frac{\pi}{2}$ compared to the N - \overline{G}'' curve, while their amplitudes are roughly equivalent. We can predict the N - \overline{G}_v curve by shifting the N - \overline{G}'' curve by a quarter wavelength. As $|s|$ approaches s_{max} , the difference between $\hat{f}_{+,0}$ and $\hat{f}_{-,0}$ diminishes, making Eq. (14) no longer a good connection representation. However, as $|s|$ increases, $|\lambda|$ diminishes, resulting in a lower transmission rate, as illustrated in Fig. 6. Refer to Appendix A about this relation between s and $|\lambda|$. Consequently, the effect of large $|s|$ has a negligible impact on G , and the exact results show good agreement in Fig. 7, justifying the approximation $\rho_{\tau,l} \simeq \omega^2$ used in Eq. (17).

We rigorously calculate the conductance G of a double junction using the $\gamma_1\gamma_3\gamma_4$ -model to verify the VB that occurs when connecting VF with opposite polarities. Using integer N_1 , N_2 , and L , the lengths of the two bilayer regions are represented as $N_1 - 2$, $N_2 - 2$, and the length of the central monolayer region is defined by $L + 2$ with $\frac{a}{2}$ as the unit. Figure 8 displays the results in case L is 80, 81, and 82. In Fig. 8 (a), the thin lines correspond to the double \downarrow junction with $(N_1, N_2) = (28, 29)$, while the thick lines correspond to the double \uparrow junction with $(N_1, N_2) = (37, 38)$. The corresponding \overline{G}_v pointed by arrows in Fig. 7 suggest that the VB occurs in Fig. 8 (a). The VB actually occurs across the entire gap for the dashed thick lines with non-zero $\text{mod}(L)$. The absence of φ in Eq. (33) allows the suppression of T for only one valley throughout the whole gap, as shown in the insets of Fig. 6. However, when $\text{mod}(L) = 0$, valley-preserving transmission, which was ignored in the analytical expression, resonates in the central single layer, disrupting the VB in the solid thick line. The main panels of Fig. 6 exemplify that the φ limits the suppression of T to an energy region much narrower than the gap width Δ in the \downarrow junction. This is why the VB is unclear in the thin lines compared to the thick dashed lines.

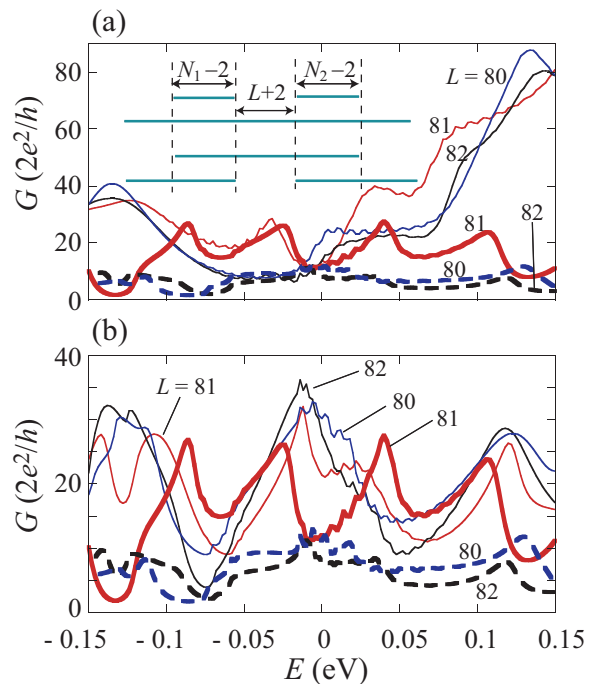


FIG. 8. The conductance of double junctions is calculated using the Landauer formula for cases where the integer L , representing the length of the central monolayer region, is 80, 81, and 82. The attached numbers indicate L . As in Fig. 7, $N_y = 1000$. Inset: Side view of the double junctions. The top layer is removed for $j \leq 0$ and $N_1 + N_2 + L \leq j$, where $x = \frac{a}{2}j$. In the double \downarrow (\uparrow) junction, the top (bottom) layer is removed in the range $N_1 \leq j \leq N_1 + L$. (a) The thin lines correspond to the double \downarrow junction ($N_1 = 28, N_2 = 29$) and the thick lines correspond to the double \uparrow junction ($N_1 = 37, N_2 = 38$). (b) The thick lines represent the same data as the thick lines in (a). The thin lines correspond to the double \uparrow junction ($N_1 = 37, N_2 = 39$).

In Fig. 8 (b), thin lines represent the G of the double \uparrow junction with $(N_1, N_2) = (37, 39)$, and thick lines from Fig. 8 (a) are re-displayed. The two double \uparrow junctions differ by only one in N_2 . In the case where $N_2 = 39$, the right \uparrow junction lacks valley selectivity and thus does not exhibit VB. Merely changing the thickness of the energy barrier by $\frac{a}{2}$ results in a difference in the presence or absence of the VB. Regarding the effect of L , only whether $\text{mod}(L)$ is zero or not is related to the VB in double \uparrow junctions. The VB does not appear in double \downarrow junctions irrespective of L .

The system's width N_y is 1000 in Figs. 7 and 8. Since k_y is discretized with a spacing $\Delta k_y = 2\pi/(\sqrt{3}aN_y)$, the channel number changes discontinuously each time E changes by $|\gamma_0|\frac{\sqrt{3}}{2}a\Delta k_y$. This leads to the fine oscillations with a period of about 0.01 eV in Fig. 8. The amplitude of these fine oscillations is, at most, approximately $2e^2/h$, demonstrating that the chosen N_y is sufficiently large for $\frac{G}{N_y}$ to become independent of N_y . In Ref. [63],

side electrodes were proposed for decomposing G into k_y components to realize VF. For the VB discussed here, k_y decomposition is unnecessary.

The incident electrons split into upper and lower waves at the entrance, as shown in Eq. (24). Simultaneously, even if the electrons are incident from a single valley, they are transformed into a superposition of opposite valley states, as indicated by Eq. (20). When the two-layer waves merge back into the single-layer wave and return to a single valley state at the exit, a phase shift of $\frac{\pi}{2}$ occurs compared to the entrance. These properties are identical between the two types of junctions. The β^{-1} appears only in the lower layer in Eqs. (24) and (25). In the \downarrow junction, electrons departing from the source electrode can reach the drain electrode without traversing between layers. Nevertheless, they inevitably experience the effect of β due to the aforementioned wave splitting and merging, resulting in an energy asymmetry in the transmission rate. In the \uparrow junction, electrons must traverse between layers, leading to additional effects of β compared to the \downarrow junction. This additional effect cancels out the effect of β present in the \downarrow junction, resulting in no observable effect of β in the \uparrow junction. This self-cancellation of β is enforced by the energy symmetry inherent in the \uparrow junction.

In the pn junction of a zigzag graphene ribbon, valley-reversed transmission similar to the \uparrow junction also occurs, but it is irrelevant to β due to the monolayer structure [62]. We assume a defect-free armchair edge at the boundary between the monolayer and bilayer regions. Defects introduced at this boundary degrade the VF. For example, if a carbon dimer is adsorbed at the boundary, the local increase in N renders N undefined. Reference [68] demonstrated that as long as the line density of these carbon dimers is low and N remains nearly constant, and the VF is maintained. Bottom-up synthesis methods based on chemical synthesis, which are effective in producing edges with minimal defects, are rapidly advancing and are expected to enable the detection of the β -effect proposed in this paper [104, 105].

VII. CONCLUSION

We derived analytical expressions for the transmission rates of two types (\downarrow and \uparrow) of partially contacted graphene in the energy gap region induced by a vertical electric field. The derivation uses the γ_1 -model, assuming that the gap width is close to the interlayer transfer integral. As the transverse wave number k_y deviates from zero, the longitudinal decay length decreases, making the transmission dominated by channels with k_y close to zero. We compared the analytical expressions with exact numerical calculations obtained from the $\gamma_1\gamma_3\gamma_4$ -model to verify the analytical expressions. In the bilayer regions, the component of the wave vector in the propagation direction becomes complex. However, we performed valley-resolved transmission rate analysis using the real part

of this component. In the \downarrow junction, valley-conserving transmission rates dominate. In the \uparrow junction, valley-reversing transmission rates are predominant. Regarding the length N of the bilayer region, the transmission rate exhibited attenuation and oscillations attributable to the valley.

We also calculated the valley conductance G_v and the total conductance G by summing the transmission rates over all subbands k_y . When comparing the \downarrow and \uparrow junctions with a common N at the center of the gap, the sign of G_v is identical in most cases; however, the curvature of the N - G curve has opposite signs. Through the chiral operation, π rotation, and probability conservation, we proved that the valley-reversing transmission rate of the \uparrow junction is an even function of the energy E . This energy symmetry enables the VB to cross the entire energy gap in the double \uparrow junction. The effect of the interlayer wave function ratio β in the wave function is diminished in the \uparrow junction compared to the \downarrow junction due to the self-cancellation effect of β , which is mandated by the energy symmetry.

Appendix A: Note on Eq. (12)

In the square root $\sqrt{A} = e^{i\frac{\theta}{2}}\sqrt{|A|}$ of a complex number $A = |A|e^{i\theta}$, we choose the range of the phase θ as $-\pi < \theta \leq \pi$. Under this standard definition,

$$\sqrt{-1 + o_1 \pm io_2} \simeq \frac{o_2}{2} \pm i \left(1 - \frac{o_1}{2}\right) \quad (\text{A1})$$

holds when $|o_1| \ll 1$ and $0 < o_2 \ll 1$. Using Eqs. (12) and (A1) with condition $|\varepsilon|, |E|, \gamma_1 \ll 1 (= |\gamma_0|)$, we obtain

$$\lambda_{\tau,l} \simeq \left(1 - \frac{\chi_- - li\chi_+}{\sqrt{3+s^2}}\right) \left(-\frac{c}{2} + \tau li \frac{\sqrt{3+s^2}}{2}\right) \quad (\text{A2})$$

where $c = \sqrt{1-s^2}$,

$$\sqrt{p-s^2+iq} = \chi_+ + i\chi_-, \quad (\text{A3})$$

and

$$\chi_{\pm} = \frac{1}{\sqrt{2}} \sqrt{\sqrt{(p-s^2)^2 + q^2} \pm p \mp s^2}. \quad (\text{A4})$$

Since $|s|$ cannot exceed Eq. (11), $|\lambda_{\tau,l}| \simeq |\lambda_{\tau}|e^{il\tau\frac{2}{3}\pi}$, and $|\lambda_{\tau}| \simeq 1 - \frac{2\chi_-}{\sqrt{3+s^2}} < 1$. An increase in $|s|$ leads to an increase in χ_- , thereby causing a decrease in $|\lambda_{\tau,l}|$.

Appendix B: Scattering matrixes for the \downarrow and \uparrow junctions

Using matrixes S_{\downarrow} and S_{\uparrow} of Refs. [37] and [68], we derive Eq. (29). S_{\downarrow} is responsible to the left transition

($j = 0$) as

$$\begin{pmatrix} \vec{\eta}^{(+)} \\ \vec{\xi}^{(-)} \end{pmatrix} = S_{\downarrow} \begin{pmatrix} \vec{\eta}^{(-)} \\ \vec{\xi}^{(+)} \end{pmatrix} \quad (\text{B1})$$

where $\vec{\eta}^{(\pm)} = (\eta_{+,+}^{(\pm)}, \eta_{-,+}^{(\pm)}, \eta_{+,-}^{(\pm)}, \eta_{-,-}^{(\pm)})$. At the right transition ($j = N$),

$$\begin{pmatrix} \vec{\eta}^{(-)} \\ \vec{\xi}^{(+)} \end{pmatrix} = S_{\bullet} \begin{pmatrix} \vec{\eta}^{(+)} \\ \vec{\xi}^{(-)} \end{pmatrix}. \quad (\text{B2})$$

In the \uparrow junction, $\bullet = \uparrow$ and $S_{\bullet} \neq S_{\downarrow}$. In the zero- k_y case, Refs. [37] and [68] indicate that

$$\begin{aligned} S_{\downarrow} &= \begin{pmatrix} \frac{\alpha_+^2}{v_+} & \frac{-\alpha_+\alpha_-}{v_+} & \frac{\alpha_+}{v_+} \\ \frac{-\alpha_+\alpha_-}{v_-} & \frac{\alpha_-^2}{v_-} & \frac{-\alpha_-}{v_-} \\ \alpha_+ & -\alpha_- & 1 \end{pmatrix} \otimes \frac{u_+}{\zeta_{\downarrow,+}} \\ &+ \begin{pmatrix} \frac{1}{v_+} & \frac{1}{v_+} & \frac{1}{v_+} \\ \frac{1}{v_-} & \frac{1}{v_-} & \frac{1}{v_-} \\ 1 & 1 & 1 \end{pmatrix} \otimes \frac{u_-}{\zeta_{\downarrow,-}} - \mathbf{1}_6 \end{aligned} \quad (\text{B3})$$

where $\mathbf{1}_n$ denotes an n -dimensional identity matrix,

$$u_{\pm} = \begin{pmatrix} 1 & \pm 1 \\ \pm 1 & 1 \end{pmatrix} \quad (\text{B4})$$

$$v_{\pm} = \frac{\alpha_{\pm}}{\beta_{\mp}}(\beta_- - \beta_+) \quad (\text{B5})$$

$$\zeta_{\downarrow,\pm} = 1 + \frac{\alpha_{\pm}^{\pm 1}\beta_- + \alpha_{\mp}^{\pm 1}\beta_+}{\beta_- - \beta_+}, \quad (\text{B6})$$

$$\alpha_{\pm} = \begin{cases} \frac{E+\varepsilon}{\sqrt{p\pm Q}} \frac{E}{|E|} & \dots & |\varepsilon| > |E| > \Delta \\ \frac{E+\varepsilon}{\sqrt{p\pm iq}} & \dots & \Delta > |E| \end{cases} \quad (\text{B7})$$

$$\beta_{\pm} = \begin{cases} \frac{2\varepsilon E \mp Q}{\gamma_1(E-\varepsilon)} & \dots & |\varepsilon| > |E| > \Delta \\ \frac{2\varepsilon E \mp iq}{\gamma_1(E-\varepsilon)} & \dots & \Delta > |E| \end{cases} \quad (\text{B8})$$

and $Q = \sqrt{(4\varepsilon^2 + \gamma_1^2)(E^2 - \Delta^2)}$. When $s = 0$ and $|E| < \Delta$, $f_{+, \downarrow, \pm}$ and Eq. (10) coincide with Eqs. (B7) and (B8), respectively. Replacement of iq to Q is the analytic continuation from the gap region $|E| < \Delta$ to the band region $\Delta < |E| < |\varepsilon|$. Replacing ε with $-\varepsilon$ in Eqs. (B5), (B6), (B7), and (B8), we obtain $v'_{\pm}, \zeta_{\uparrow,\pm}, \alpha'_{\pm}, \beta'_{\pm}$, and

$$S_{\uparrow} = \begin{pmatrix} \frac{\alpha_+^2}{v'_+} & \frac{-\alpha'_+\alpha'_-}{v'_+} \frac{\beta'_+}{\beta'_-} & \frac{\alpha'_+}{v'_+} \beta'_+ \\ \frac{-\alpha'_+\alpha'_-}{v'_-} \frac{\beta'_-}{\beta'_+} & \frac{\alpha_-^2}{v'_-} & \frac{-\alpha'_-}{v'_-} \beta'_- \\ \frac{\alpha'_+}{\beta'_+} & -\frac{\alpha'_-}{\beta'_-} & 1 \end{pmatrix} \otimes \frac{u_+}{\zeta_{\uparrow,+}}$$

$$+ \begin{pmatrix} \frac{1}{v'_+} & \frac{\beta'_+}{v'_+\beta'_-} & \frac{1}{v'_+} \beta'_+ \\ \frac{\beta'_-}{v'_-\beta'_+} & \frac{1}{v'_-} & \frac{1}{v'_-} \beta'_- \\ \frac{1}{\beta'_+} & \frac{1}{\beta'_-} & 1 \end{pmatrix} \otimes \frac{u_-}{\zeta_{\uparrow,-}} - \mathbf{1}_6 \quad (\text{B9})$$

Useful formulas are $\beta'_{\pm} = \frac{1}{\beta_{\pm}}$ and $\beta_+\beta_- = \frac{\varepsilon+E}{\varepsilon-E} = -\frac{\alpha_{\pm}}{\alpha'_{\pm}}$.

When $|\varepsilon| > |E| > \Delta$, v_{\pm} is proportional to the probability flow of mode $\eta_{\tau,\pm}$, and the normalized scattering matrix $\bar{S}_o = VS_oV^{-1}$ becomes the 6-dimensional unitary matrix, where

$$V = \begin{pmatrix} \sqrt{v_+} & 0 & 0 \\ 0 & \sqrt{v_-} & 0 \\ 0 & 0 & 1 \end{pmatrix} \otimes \mathbf{1}_2. \quad (\text{B10})$$

When $\Delta > |E|$ and the length of the bilayer region becomes infinite, there is perfect reflection of an incident wave from the monolayer region, and the (3,3) block $\zeta_{o,+}^{-1}u_+ + \zeta_{o,-}^{-1}u_- - \mathbf{1}_2$ becomes the two-dimensional unitary matrix. Correspondence between Eq. (27) and S_o is as follows. r_o consists of the (1,1), (1,2), (2,1) and (2,2) blocks of S_o . t_{\downarrow} includes the (1,3) and (2,3) blocks of S_{\downarrow} . \tilde{t}_{\bullet} is composed of the (3,1) and (3,2) blocks of S_{\bullet} .

In the following, we consider only the gapped region, $\Delta > |E|$. Applying Eqs. (B3) and (B9) to Eq. (28), we obtain

$$T_{\nu',\nu} = \frac{\gamma_1^2}{q^2} \left| \sum_{\tau=\pm} \frac{(E+\varepsilon)Y_{\nu',\nu}^{(\tau)}}{\zeta_{\bullet,+}\zeta_{\bullet,-}\zeta_{\downarrow,+}\zeta_{\downarrow,-}} \right|^2 \quad (\text{B11})$$

where

$$\begin{aligned} Y_{\nu',\nu}^{(\tau)} &= \zeta_{\downarrow,-}^2 \text{Re} \left(\frac{\alpha}{\beta} \lambda_{\tau}^N \right) + \nu\nu' \zeta_{\downarrow,+}^2 \text{Re} \left(\frac{\lambda_{\tau}^N}{\alpha\beta} \right) \\ &+ 2\nu\delta_{\nu',\nu} \zeta_{\downarrow,+} \zeta_{\downarrow,-} \tau \text{Re} \left(\frac{\lambda_{\tau}^N}{\beta} \right) \end{aligned} \quad (\text{B12})$$

for the \downarrow junction, and

$$\begin{aligned} Y_{\nu',\nu}^{(\tau)} &= \zeta_{\downarrow,-} \zeta_{\uparrow,-} \text{Re} (\alpha' \lambda_{\tau}^N) + \nu\nu' \zeta_{\downarrow,+} \zeta_{\uparrow,+} \text{Re} \left(\frac{\lambda_{\tau}^N}{\alpha} \right) \\ &+ \left(\nu \zeta_{\uparrow,-} \zeta_{\downarrow,+} + \frac{\alpha'}{\alpha} + \nu' \zeta_{\uparrow,+} \zeta_{\downarrow,-} \right) \tau \text{Re} (\lambda_{\tau}^N) \end{aligned} \quad (\text{B13})$$

for the \uparrow junction with abbreviation $\beta = \beta_+$, $\alpha = \alpha_+$ and $\alpha' = \alpha'_+$. When $|\varepsilon| \gg \gamma_1$, all the ζ 's are close to $1 - 2i|\varepsilon|\frac{E}{q}$, and $(\alpha, \alpha') \simeq \frac{\varepsilon}{|\varepsilon|}(\alpha_0, \alpha'_0)$, where $\alpha_0 \equiv \frac{|E+\varepsilon|}{\sqrt{p}}$, and $\alpha'_0 \equiv \frac{\varepsilon}{|\varepsilon|} \frac{E-\varepsilon}{\sqrt{p}}$. It follows approximations

$$Y_{\nu',\nu}^{(\tau)} = \left(1 - 2i|\varepsilon|\frac{E}{q}\right)^2 \left[\left(\sqrt{\alpha_0} + \frac{\varepsilon}{|\varepsilon|}\frac{\tau\nu}{\sqrt{\alpha_0}}\right)^2 \delta_{\nu',\nu} + \left(\alpha_0 - \frac{1}{\alpha_0}\right) \delta_{\nu',-\nu} \right] \frac{\varepsilon}{|\varepsilon|} \text{Re} \left(\frac{\lambda_\tau^N}{\beta} \right) \quad (\text{B14})$$

for Eq. (B12), and

$$Y_{\nu',\nu}^{(\tau)} = \left(1 - 2i|\varepsilon|\frac{E}{q}\right)^2 \left[\left(\alpha'_0 + \frac{1}{\alpha_0} + \frac{\varepsilon}{|\varepsilon|}\tau\nu\frac{2E}{E+\varepsilon}\right) \delta_{\nu',\nu} + \left(\alpha'_0 - \frac{1}{\alpha_0} - \frac{\varepsilon}{|\varepsilon|}\tau\nu\frac{2\varepsilon}{E+\varepsilon}\right) \delta_{\nu',-\nu} \right] \frac{\varepsilon}{|\varepsilon|} \text{Re} (\lambda_\tau^N) \quad (\text{B15})$$

for Eq. (B13).

Since $|E| \ll |\varepsilon|$, $\alpha_0 > 0$, and $\alpha'_0 < 0$, the terms satisfying Eq. (14) dominate Eqs. (B14) and (B15). In comparison with Eq. (29), $|Y^{(+)} + Y^{(-)}|$ equals $\frac{\gamma_1^2}{q^2}|\varepsilon - E||Z|$ in these dominant terms.

The substitution of the ζ with $1 - 2i|\varepsilon|\frac{E}{q}$ is limited to Y and is not performed in the denominator $\zeta_{\bullet,+}\zeta_{\bullet,-}\zeta_{\downarrow,+}\zeta_{\downarrow,-}$ in Eq. (B11). Had the substitution been performed in

the denominator as well, the accuracy of the derived analytical expression would have been compromised. This substitution was used within the minimal necessary extent to reproduce the Re factors in Eqs. (25) and (26). Regardless of whether Eqs. (B13) or (B15) is used, Eq. (B11) satisfies the symmetry (41) owing to Eq. (42).

-
- [1] A. B. Balantekin and N. Takigawa, Quantum tunneling in nuclear fusion, *Rev. Mod. Phys.* **70**, 77 (1998).
- [2] G. Binnig and H. Rohrer, Scanning tunneling microscopy from birth to adolescence, *Rev. Mod. Phys.* **59**, 615 (1987).
- [3] L. Esaki, Long journey into tunneling, *Rev. Mod. Phys.* **46**, 237 (1974).
- [4] A. Fert, Nobel Lecture: Origin, development, and future of spintronics, *Rev. Mod. Phys.* **80**, 1517 (2008).
- [5] T. Scheike, Z. Wen, H. Sukegawa, and S. Mitani, 631% room temperature tunnel magnetoresistance with large oscillation effect in CoFe/MgO/CoFe(001) junctions, *Appl. Phys. Lett.* **122**, 112404 (2023).
- [6] F. Xu, A. Sadrzadeh, Z. Xu, and B. I. Yakobson, Can carbon nanotube fibers achieve the ultimate conductivity? Coupled-mode analysis for electron transport through the carbon nanotube contact, *J. Appl. Phys.* **114**, 063714 (2013).
- [7] R. Tamura, Valley Current Filtering and Reversal by Parallel Side Contacted Armchair Nanotubes, *J. Phys. Soc. Jpn.* **90**, 114701 (2021).
- [8] J. Zheng, P. Guo, Z. Ren, Z. Jiang, J. Bai, and Z. Zhang, Conductance fluctuations as a function of sliding motion in bilayer graphene nanoribbon junction: A first-principles investigation, *Appl. Phys. Lett.* **101**, 083101 (2012).
- [9] D. Yin, W. Liu, X. Li, L. Geng, X. Wang, and P. Huai, Mono-bi-monolayer graphene junction introduced quantum transport channels, *Appl. Phys. Lett.* **103**, 173519 (2013).
- [10] Y. Wang, Transfer matrix theory of monolayer graphene/bilayer graphene heterostructure superlattice, *J. Appl. Phys.* **116**, 164317 (2014).
- [11] D. Valencia, J.-Q. Lu, J. Wu, F. Liu, F. Zhai, and Y.-J. Jiang, Electronic transmission in graphene suppressed by interlayer interference, *AIP Advances* **3**, 102125 (2013).
- [12] V. Torres, D. Faria, and A. Latge, Exploring valley polarized transport in graphene bilayer flakes, *Physica B* **666**, 415148 (2023).
- [13] C. J. Paez, A. L. C. Pereira, J. N. B. Rodrigues, and N. M. R. Peres, Electronic transport across linear defects in graphene, *Phys. Rev. B* **92**, 045426 (2015).
- [14] H. Z. Olyaei, P. Ribeiro, and E. V. Castro, Transmission across a bilayer graphene region, *Phys. Rev. B* **99**, 205436 (2019).
- [15] J. Nilsson, A. H. Castro Neto, F. Guinea, and N. M. R. Peres, Transmission through a biased graphene bilayer barrier, *Phys. Rev. B* **76**, 165416 (2007).
- [16] T. Nakanishi, M. Koshino, and T. Ando, Transmission through a boundary between monolayer and bilayer graphene, *Phys. Rev. B* **82**, 125428 (2010).
- [17] R. Li, Z. Lin, and K. S. Chan, Intervalley conversion in bilayer-monolayer graphene junctions, *Physica E* **113**, 109 (2019).
- [18] H. Li, H. Li, Y. Zheng, and J. Niu, Electron transport of step-shaped graphene nanoribbon, *Physica B* **406**, 1385 (2011).
- [19] K. M. M. Habib, F. Zahid, and R. K. Lake, Negative differential resistance in bilayer graphene nanoribbons, *Appl. Phys. Lett.* **98**, 192112 (2011).
- [20] J. W. Gonzalez, H. Santos, E. Prada, L. Brey, and L. Chico, Gate-controlled conductance through bilayer graphene ribbons, *Phys. Rev. B* **83**, 205402 (2011).
- [21] J. W. Gonzalez, H. Santos, M. Pacheco, L. Chico, and L. Brey, Electronic transport through bilayer graphene flakes, *Phys. Rev. B* **81**, 195406 (2010).
- [22] E. Cannavo, D. Marian, E. G. Marin, G. Iannaccone, and G. Fiori, Transport properties in partially overlapping van der Waals junctions through a multiscale investigation, *Phys. Rev. B* **104**, 085433 (2021).
- [23] N. Benlakhrouy, A. Jellal, and M. Schreiber, Transport properties of hybrid single-bilayer graphene interfaces in a magnetic field, *Phys. Rev. B* **108** (2023).
- [24] H. M. Abdullah, B. V. Duppen, M. Zarenia, H. Bahlouli, and F. M. Peeters, Quantum transport across van der Waals domain walls in bilayer graphene, *Journal of Physics: Condensed Matter* **29**, 425303 (2017).

- [25] N. Benlakhrouy and A. Jellal, Tunneling conductance of hybrid bilayer-single graphene junctions, *Phys. Scr.* **99**, 075920 (2024).
- [26] M. Mirzakhani, N. Myoung, F.M. Peeters, and H.C. Park, Electronic Mach-Zehnder interference in a bipolar hybrid monolayer-bilayer graphene junction, *Carbon* **201**, 734 (2023).
- [27] E. McCann, Asymmetry gap in the electronic band structure of bilayer graphene, *Phys. Rev. B* **74**, 161403(R) (2006).
- [28] J. Ruseckas, G. Juzeliunas, and I. V. Zozoulenko, Spectrum of electrons in bilayer graphene nanoribbons and nanotubes: An analytical approach, *Phys. Rev. B* **83**, 035403 (2011).
- [29] Y. Shimazaki, M. Yamamoto, I. V. Borzenets, K. Watanabe, T. Taniguchi and S. Tarucha, Generation and detection of pure valley current by electrically induced Berry curvature in bilayer graphene, *Nat. Phys.* **11**, 1032 (2015).
- [30] M. Sui, G. Chen, L. Ma, W. Shan, D. Tian, K. Watanabe, T. Taniguchi, X. Jin, W. Yao, D. Xiao, and Y. Zhang, Gate-tunable topological valley transport in bilayer graphene, *Nat. Phys.* **11**, 1027 (2015).
- [31] K. Kim, M. Yankowitz, B. Fallahazad, S. Kang, H. C. Movva, S. Huang, S. Larentis, C. M. Corbet, T. Taniguchi, K. Watanabe, S. K. Banerjee, B. J. LeRoy, and E. Tutuc, van der Waals Heterostructures with High Accuracy Rotational Alignment, *Nano Lett* **16**, 1989 (2016).
- [32] J. Yan and M. S. Fuhrer, Charge transport in dual gated bilayer graphene with Corbino geometry, *Nano Lett* **10**, 4521 (2010).
- [33] J. Yin, C. Tan, D. Barcons-Ruiz, I. Torre, K. Watanabe, T. Taniguchi, J. C. W. Song, J. Hone, and F. H. L. Koppens, Tunable and giant valley-selective Hall effect in gapped bilayer graphene, *Science* **375**, 1398 (2022).
- [34] J. Li, R.-X. Zhang, Z. Yin, J. Zhang, K. Watanabe, T. Taniguchi, and J. Z. C. Li, A valley valve and electron beam splitter, *Science* **362**, 1149 (2018).
- [35] C.-S. Park, Band-Gap tuned oscillatory conductance in bilayer graphene n-p-n junction, *J. Appl. Phys.* **116**, 033702 (2014).
- [36] B. V. Duppen and F. M. Peeters, Four-band tunneling in bilayer graphene, *Phys. Rev. B* **87**, 205427 (2013).
- [37] R. Tamura, Tunnel Valley Current Filter in the Partially Overlapped Graphene under the Vertical Electric Field, *J. Phys. Soc. Jpn.* **92**, 123704 (2023).
- [38] T. Kawarabayashi and Y. Hatsugai, Bulk-edge correspondence with generalized chiral symmetry, *Phys. Rev. B* **103**, 205306 (2021).
- [39] H. Nakai, M. Kawano, and C. Hotta, Uncovering hidden chiral symmetry in non bipartite kagome and pyrochlore lattices with spin-orbit coupling by the Wilson loop, *Phys. Rev. B* **108**, L081106 (2023).
- [40] D. Xiao, W. Yao, and Q. Niu, Valley-contrasting physics in graphene: magnetic moment and topological transport, *Phys. Rev. Lett.* **99**, 236809 (2007).
- [41] R. V. Gorbachev, J. C. W. Song, G. L. Yu, A. V. Kretinin, F. Withers, Y. Cao, A. Mishchenko, I. V. Grigorieva, K. S. Novoselov, L. S. Levitov, and A. K. Geim, Detecting topological currents in graphene superlattices, *Science* **346**, 448 (2014).
- [42] J. H. J. Martiny, K. Kaasbjerg, and A.-P. Jauho, Tunable valley Hall effect in gate-defined graphene superlattices, *Phys. Rev. B* **100**, 155414 (2019).
- [43] K. Endo, K. Komatsu, T. Iwasaki, E. Watanabe, D. Tsuya, K. Watanabe, T. Taniguchi, Y. Noguchi, Y. Wakayama, Y. Morita, and S. Moriyama, Topological valley currents in bilayer graphene/hexagonal boron nitride superlattices, *Appl. Phys. Lett.* **114**, 243105 (2019).
- [44] K. Komatsu, Y. Morita, E. Watanabe, D. Tsuya, K. Watanabe, T. Taniguchi, and S. Moriyama, Observation of the quantum valley Hall state in ballistic graphene superlattices, *Sci. Adv.* **4**, eaaq0194 (2018).
- [45] S. M. Settnes, S. R. Power, M. Brandbyge, and A. P. Jauho, Graphene Nanobubbles as Valley Filters and Beam Splitters, *Phys. Rev. Lett.* **117**, 276801 (2016).
- [46] J. L. Garcia-Pomar, A. Cortijo, and M. Nieto-Vesperinas, Fully Valley-Polarized Electron Beams in Graphene, *Phys. Rev. Lett.* **100**, 236801 (2008).
- [47] L. E. Golub, S. A. Tarasenko, M. V. Entin, and L. I. Margarill, Valley separation in graphene by polarized light, *Phys. Rev. B* **84**, 195408 (2011).
- [48] L. E. Golub and S. A. Tarasenko, Valley polarization induced second harmonic generation in graphene, *Phys. Rev. B* **90**, 201402(R) (2014).
- [49] S. A. Oliaei Motlagh, F. Nematollahi, V. Apalkov, and M. I. Stockman, Topological resonance and single-optical-cycle valley polarization in gapped graphene, *Phys. Rev. B* **100**, 115431 (2019).
- [50] L.-L. Chang, Q.-P. Wu, Y.-Z. Li, R.-L. Zhang, M.-R. Liu, W.-Y. Li, F.-F. Liu, X.-B. Xiao, and Z.-F. Liu, Pure valley-polarized current in graphene junction induced by circularly polarized light and carrier mass, *Physica E* **130**, 114681 (2021).
- [51] A. Friedlan and M. M. Dignam, Valley polarization in biased bilayer graphene using circularly polarized light, *Phys. Rev. B* **103**, 075414 (2021).
- [52] M. S. Mrudul, A. Jimenez-Galan, M. Ivanov, and G. Dixit, Light-induced valleytronics in pristine graphene, *Optica* **8**, 422 (2021).
- [53] H. K. Kelardeh, U. Saalman, and J. M. Rost, Ultra-short laser-driven dynamics of massless Dirac electrons generating valley polarization in graphene, *Phys. Rev. Research* **4**, L022014 (2022).
- [54] A. J. Zafar, A. Mitra, and V. Apalkov, Ultrafast valley polarization of graphene nanorings, *Phys. Rev. B* **106**, 155147 (2022).
- [55] H. Santos, L. Chico, and L. Brey, Carbon nanoelectronics: unzipping tubes into graphene ribbons, *Phys. Rev. Lett.* **103**, 086801 (2009).
- [56] S. Tapar and B. Muralidharan, Effectuating tunable valley selection via multiterminal monolayer graphene devices, *Phys. Rev. B* **107**, 205415 (2023).
- [57] H. Schomerus, Helical scattering and valleytronics in bilayer graphene, *Phys. Rev. B* **82**, 165409 (2010).
- [58] Y. S. Ang, S. A. Yang, C. Zhang, Z. Ma, and L. K. Ang, Valleytronics in merging Dirac cones: All-electric-controlled valley filter, valve, and universal reversible logic gate, *Phys. Rev. B* **96**, 245410 (2017).
- [59] T. Fujita, M. B. A. Jalil, and S. G. Tan, Valley filter in strain engineered graphene, *Appl. Phys. Lett.* **97**, 043508 (2010).
- [60] Z. Feng, Z. Xiaofang, C. Kai, and H. Q. Xu, Magnetic barrier on strained graphene: A possible valley filter, *Phys. Rev. B* **82**, 115442 (2010).
- [61] Z. Feng and C. Kai, Valley filtering in graphene with a

- Dirac gap, *Phys. Rev. B* **85**, 155415 (2012).
- [62] A. R. Akhmerov, J. H. Bardarson, R. A. and C. W. J. Beenakker, Theory of the valley-valve effect in graphene nanoribbons, *Phys. Rev. B* **77**, 205416 (2008).
- [63] V. H. Nguyen, S. Dechamps, P. Dollfus, and J.-C. Charlier, Valley Filtering and Electronic Optics Using Polycrystalline Graphene, *Phys. Rev. Lett.* **117**, 247702 (2016).
- [64] A. Rycerz, J. Tworzyd, and C. W. J. Beenakker, Valley filter and valley valve in graphene, *Nat. Phys.* **3**, 172 (2007).
- [65] J.-H. Chen, G. Autes, N. Alem, F. Gargiulo, A. Gautam, M. Linck, C. Kisielowski, O. V. Yazyev, S. G. Louie, and A. Zettl, Controlled growth of a line defect in graphene and implications for gate-tunable valley filtering, *Phys. Rev. B* **89**, 121407(R) (2014).
- [66] S. K. Wang and J. Wang, Valley precession in graphene superlattices, *Phys. Rev. B* **92**, 075419 (2015).
- [67] J. J. Wang, S. Liu, J. Wang, and J.-F. Liu, Valley-coupled transport in graphene with Y-shaped Kekule structure, *Phys. Rev. B* **98**, 195436 (2018).
- [68] R. Tamura, Origins of Valley Current Reversal in Partially Overlapped Graphene Layers, *J. Phys. Soc. Jpn.* **92**, 114706 (2023).
- [69] W. Yao, S. A. Yang, and Q. Niu, Edge states in graphene: from gapped flat-band to gapless chiral modes, *Phys. Rev. Lett.* **102**, 096801 (2009).
- [70] V. S. Prudkovski, Y. Hu, K. Zhang, Y. Hu, P. Ji, G. Nunn, J. Zhao, C. Shi, A. Tejada, D. Wander, A. D. Cecco, C. B. Winkelmann, Y. Jiang, T. Zhao, K. Wakabayashi, Z. Jiang, L. Ma, C. Berger, and W. A. de Heer, An epitaxial graphene platform for zero-energy edge state nanoelectronics, *Nat Commun* **13**, 7814 (2022).
- [71] J. Li, I. Martin, M. Buttiker, and A. F. Morpurgo, Topological origin of subgap conductance in insulating bilayer graphene, *Nat. Phys.* **7**, 38 (2010).
- [72] E. V. Castro, N. M. Peres, J. M. Lopes dos Santos, A. H. Neto, and F. Guinea, Localized states at zigzag edges of bilayer graphene, *Phys. Rev. Lett.* **100**, 026802 (2008).
- [73] K. Davydov, X. Zhang, W. Ren, M. Coles, L. Kline, B. Zucker, K. Watanabe, T. Taniguchi, and K. Wang, Easy-to-configure zero-dimensional valley-chiral modes in a graphene point junction, *Sci. Adv.* **10**, eadp6296 (2024).
- [74] Z. Qiao, J. Jung, Q. Niu, and A. H. Macdonald, Electronic highways in bilayer graphene, *Nano Lett.* **11**, 3453 (2011).
- [75] I. Martin, Y. M. Blanter, and A. F. Morpurgo, Topological confinement in bilayer graphene, *Phys. Rev. Lett.* **100**, 036804 (2008).
- [76] J. Jeil, Z. Fan, Q. Zhenhua, and H. M. Allan, Valley-Hall kink and edge states in multilayer graphene, *Phys. Rev. B* **84**, 075418 (2011).
- [77] S. G. Cheng, H. Liu, H. Jiang, Q. F. Sun, and X. C. Xie, Manipulation and Characterization of the Valley-Polarized Topological Kink States in Graphene-Based Interferometers, *Phys. Rev. Lett.* **121**, 156801 (2018).
- [78] H. Chen, P. Zhou, J. Liu, J. Qiao, B. Oezylmaz, and J. Martin, Gate controlled valley polarizer in bilayer graphene, *Nat. Commun.* **11**, 1202 (2020).
- [79] J. Li, K. Wang, K. J. McFaul, Z. Zern, Y. Ren, K. Watanabe, T. Taniguchi, Z. Qiao, and J. Zhu, Gate-controlled topological conducting channels in bilayer graphene, *Nat. Nanotechnol.* **11**, 1060 (2016).
- [80] J. Lee, K. Watanabe, T. Taniguchi, H.-J. Lee, Realisation of topological zero-energy mode in bilayer graphene in zero magnetic field, *Sci. Rep.* **7**, 6466 (2017).
- [81] Z. F. A. H. MacDonald, and E. J. Mele, Valley Chern numbers and boundary modes in gapped bilayer graphene, *Proceedings of the National Academy of Sciences* **110**, 10546 (2013).
- [82] L.-J. Yin, H. Jiang, J.-B. Qiao, and L. He, Direct imaging of topological edge states at a bilayer graphene domain wall, *Nat. Commun.* **7**, 11760 (2016).
- [83] L. Ju, Z. Shi, N. Nair, Y. Lv, C. Jin, J. Velasco, C. Ojeda-Aristizabal, H. A. Bechtel, M. C. Martin, A. Zettl, J. Analytis, and F. Wang, Topological valley transport at bilayer graphene domain walls, *Nature* **520**, 650 (2015).
- [84] F. R. Geisenhof, F. Winterer, A. M. Seiler, J. Lenz, I. Martin, R. T. Weitz, Interplay between topological valley and quantum hall edge transport, *Nat. Commun.* **13**, 4187 (2022).
- [85] F. R. Geisenhof, F. Winterer, S. Wakolbinger, T. D. Gokus, Y. C. Durmaz, D. Priesack, J. Lenz, F. Keilmann, K. Watanabe, T. Taniguchi, R. Guerrero-Aviles, M. Pelc, A. Ayuela, and R. T. Weitz, Anisotropic Strain-Induced Soliton Movement Changes Stacking Order and Band Structure of Graphene Multilayers: Implications for Charge Transport, *ACS Appl. Nano Mater.* **2**, 6067 (2019).
- [86] G. W. Semenoff, V. Semenoff, and F. Zhou, Domain walls in gapped graphene, *Phys. Rev. Lett.* **101**, 087204 (2008).
- [87] S.-g. Cheng, J. Zhou, H. Jiang, and Q.-F. Sun, The valley filter efficiency of monolayer graphene and bilayer graphene line defect model, *New Journal of Physics* **18**, 129601 (2016).
- [88] Y. Hatsugai, Chern number and edge states in the integer quantum Hall effect, *Phys. Rev. Lett.* **71**, 3697 (1993).
- [89] Hatsugai, T. Fukui, and H. Aoki, Topological analysis of the quantum Hall effect in graphene: Dirac-Fermi transition across van Hove singularities and edge versus bulk quantum numbers, *Phys. Rev. B* **74**, 205414 (2006).
- [90] D. J. Thouless, M. Kohmoto, M. P. Nightingale, and M. den Nijs, Quantized Hall Conductance in a Two-Dimensional Periodic Potential, *Phys. Rev. Lett.* **49**, 405 (1982).
- [91] G. Tamaki, T. Kawakami, and M. Koshino, Topological junction states and their crystalline network in systems with chiral symmetry: Application to graphene nanoribbons, *Phys. Rev. B* **101**, 205311 (2020).
- [92] S. Ryu and Y. Hatsugai, Topological origin of zero-energy edge states in particle-hole symmetric systems, *Phys. Rev. Lett.* **89**, 077002 (2002).
- [93] B. Partoens and F. M. Peeters, From graphene to graphite: Electronic structure around the K point, *Phys. Rev. B* **74**, 075404 (2006).
- [94] J. Nilsson, A. H. Castro Neto, F. Guinea, and N. M. R. Peres, Electronic properties of bilayer and multilayer graphene, *Phys. Rev. B* **78**, 045405 (2008).
- [95] G. W. Semenoff, Condensed-Matter Simulation of a Three-Dimensional Anomaly, *Phys. Rev. Lett.* **53**, 2449 (1984).
- [96] T. Ando, Theory of Electronic States and Transport in Carbon Nanotubes, *J. Phys. Soc. Jpn.* **74**, 777 (2005).
- [97] E. McCann and V. I. Fal'ko, Landau-level degeneracy and quantum Hall effect in a graphite bilayer, *Phys.*

- Rev. Lett. **96**, 086805 (2006).
- [98] K. F. Mak, C. H. Lui, J. Shan, and T. F. Heinz, Observation of an electric-field-induced band gap in bilayer graphene by infrared spectroscopy., Phys. Rev. Lett. **102**, 256405 (2009).
- [99] Y. Zhang, T. T. Tang, C. Girit, Z. Hao, M. C. Martin, A. Zettl, M. F. Crommie, Y. R. Shen, and F. Wang, Direct observation of a widely tunable bandgap in bilayer graphene, Nature **459**, 820 (2009).
- [100] D. H. S. Silva, Band gap opening in Bernal bilayer graphene under applied electric field calculated by DFT, Physica B **694**, 416398 (2024).
- [101] Y. J. Zhang, T. Oka, R. Suzuki, J. T. Ye, and Y. Iwasa, Electrically Switchable Chiral Light-Emitting Transistor, Science **344**, 725 (2014).
- [102] R. Tamura, Perturbation calculations on interlayer transmission rates from symmetric to antisymmetric channels in parallel armchair nanotube junctions, Phys. Rev. B **99**, 155407 (2019).
- [103] M. Buttiker, Y. Imry, R. Landauer, and S. Pinhas, Generalized many-channel conductance formula with application to small rings, Phys. Rev. B **31**, 6207 (1985).
- [104] A. Kinikar, X. Xu, M. Di Giovannantonio, O. Groning, K. Eimre, C. A. Pignedoli, K. Mullen, A. Narita, P. Ruffieux, and R. Fasel, On-Surface Synthesis of Edge-Extended Zigzag Graphene Nanoribbons, Adv. Mater. **35**, 2306311 (2023).
- [105] P. Ruffieux, S. Wang, B. Yang, C. Sanchez-Sanchez, J. Liu, T. Dienel, L. Talirz, P. Shinde, C. A. Pignedoli, D. Passerone, T. Dumslaff, X. Feng, K. Mullen, and R. Fasel, On-surface synthesis of graphene nanoribbons with zigzag edge topology, Nature **531**, 489 (2016).